

# Structure and Properties of Nanocomposites Formed by the Occlusion of Block Copolymer Worms and Vesicles Within Calcite Crystals

Yi-Yeoun Kim,\* Mona Semsarilar, Joseph D. Carloni, Kang Rae Cho, Alexander N. Kulak, Iryna Polishchuk, Coit T. Hendley IV, Paul J. M. Smeets, Lee A. Fielding, Boaz Pokroy, Chiu C. Tang, Lara A. Estroff, Shefford P. Baker, Steven P. Armes, and Fiona C. Meldrum\*

This article describes an experimentally versatile strategy for producing inorganic/organic nanocomposites, with control over the microstructure at the nano- and mesoscales. Taking inspiration from biominerals,  $\text{CaCO}_3$  is coprecipitated with anionic diblock copolymer worms or vesicles to produce single crystals of calcite occluding a high density of the organic component. This approach can also be extended to generate complex structures in which the crystals are internally patterned with nano-objects of differing morphologies. Extensive characterization of the nanocomposite crystals using high resolution synchrotron powder X-ray diffraction and vibrational spectroscopy demonstrates how the occlusions affect the short and long-range order of the crystal lattice. By comparison with nanocomposite crystals containing latex particles and copolymer micelles, it is shown that the effect of these occlusions on the crystal lattice is dominated by the interface between the inorganic crystal and the organic nano-objects, rather than the occlusion size. This is supported by in situ atomic force microscopy studies of worm occlusion in calcite, which reveal flattening of the copolymer worms on the crystal surface, followed by burial and void formation. Finally, the mechanical properties of the nanocomposite crystals are determined using nanoindentation techniques, which reveal that they have hardnesses approaching those of biogenic calcites.

## 1. Introduction

The development of synthetic strategies that enable precise control over both the composition and structure of materials at the nanoscale promises the ability to generate multicomponent, nanostructured materials that display novel combinations of physical and chemical properties. A wide range of approaches have been explored to create both organic/inorganic nanocomposites and inorganic heterostructures, including layer-by-layer deposition of polyelectrolytes and inorganic nanoparticles,<sup>[1]</sup> and the vapor-phase deposition of inorganic thin films.<sup>[2]</sup> However, the possibility of generating such structures using assembly-based processes is particularly attractive. Both binary and tertiary superlattices can be generated through the coassembly of contrasting nanoparticles to give precise control over the stoichiometry and interparticle spacing,<sup>[3]</sup> and the coassembly of block

Dr. Y.-Y. Kim, Dr. A. N. Kulak, Prof. F. C. Meldrum  
School of Chemistry  
University of Leeds  
Leeds LS2 9JT, UK  
E-mail: Y.Y.Kim@leeds.ac.uk; F.Meldrum@leeds.ac.uk

Dr. M. Semsarilar, Dr. L. A. Fielding,<sup>[†]</sup> Prof. S. P. Armes  
Department of Chemistry  
The University Of Sheffield  
Sheffield S3 7HF, UK

J. D. Carloni, C. T. Hendley IV, Prof. L. A. Estroff, Prof. S. P. Baker  
Department of Materials Science and Engineering  
Cornell University  
Ithaca, NY 14853, USA

J. D. Carloni, C. T. Hendley IV, Prof. L. A. Estroff, Prof. S. P. Baker  
Kavli Institute for Nanoscale Science  
Physical Sciences Building  
Cornell University  
Ithaca, NY 14853, USA

Dr. K. R. Cho, P. J. M. Smeets  
The Molecular Foundry  
Lawrence Berkeley National Laboratory  
Berkeley, CA 94720, USA

I. Polishchuk, Prof. B. Pokroy  
Department of Materials Science and Engineering  
and the Russell Berrie Nanotechnology Institute  
Technion

Israel Institute of Technology  
Haifa 32000, Israel

Dr. C. C. Tang  
Diamond Light Source  
Harwell Science and Innovation Campus  
Didcot OX11 0DE, UK

<sup>[†]</sup>Present address: School of Materials, University of Manchester, Oxford road, Manchester M13 9PL, UK

This is an open access article under the terms of the Creative Commons Attribution License, which permits use, distribution and reproduction in any medium, provided the original work is properly cited.



DOI: 10.1002/adfm.201504292

copolymers and inorganic nanoparticles can be used to provide control over the spatial organization of the nanoparticles within the organic matrix.<sup>[4]</sup>

One of the ultimate examples of self-assembly processes is of course crystallization itself, where control over nucleation and growth is used to generate particles with defined polymorphs, morphologies, and sizes. Although crystallization is traditionally used as a means of purification, it is noted that it is possible to occlude certain “impurity species” within a crystal lattice under appropriate experimental conditions, creating a multicomponent system. The ability to dye crystals with appropriate partner dyes has been recognized for centuries,<sup>[5]</sup> where this approach has led to applications such as solid state dye lasers. A wonderful example is also provided by nature in the form of biominerals, where even single crystal biominerals are composite structures in which biomacromolecules are embedded within the crystal lattice.<sup>[6]</sup> These organic macromolecules appear to be associated with specific crystal planes,<sup>[7]</sup> and, in common with manmade composites, whose properties exceed those of the constituents, calcite biominerals are often harder than their pure synthetic counterparts.<sup>[8]</sup> Significantly, this biogenic strategy can be translated to model synthetic systems, which include the incorporation of surface-functionalized organic and inorganic nanoparticles within calcite (CaCO<sub>3</sub>),<sup>[9,10]</sup> zinc oxide,<sup>[11]</sup> and sodium chloride.<sup>[12]</sup> Recent work has also shown that amino acids can be occluded within calcite<sup>[13]</sup> and zinc oxide,<sup>[14]</sup> raising the possibility that additive occlusion within crystals may be more widespread than currently believed.

The work described in this article builds on these observations to create inorganic/organic nanocomposites that are structurally distinct from any studied previously. Profiting from our ability to generate families of polyelectrolytic diblock copolymer nano-objects by tailoring the mean degrees of polymerization of the constituent blocks, we compare the occlusion of anionic diblock copolymer worms and vesicles — bearing identical surface chemistries — within calcite crystals. These nano-objects were designed such that they exhibit anionic surface chains, which can significantly enhance occlusion rates.<sup>[9,10]</sup> The influence of the size and shape of these particles on the microstructures and mechanical properties of the resulting nanocomposite crystals are also investigated. These data are then compared with those reported for previous systems, enhancing our understanding of the design rules and structure-property relationships of these nanocomposite crystals.

## 2. Results

It is well known that diblock copolymers can self-assemble to form a wide range of morphologies.<sup>[15]</sup> Recently, polymerization-induced self-assembly (PISA) has been shown to be a highly versatile, efficient, and generic route for the formation of diblock copolymer nanoparticles in either water,<sup>[16]</sup> ethanol<sup>[17]</sup> or *n*-alkanes.<sup>[18]</sup> For example, a poly(methacrylic acid) (PMAA) chain transfer agent can be used for the reversible addition-fragmentation chain transfer polymerization of benzyl methacrylate (BzMA) in ethanol to produce well-defined diblock copolymer nanoparticles in the form of either spheres, worms

or vesicles (Figure 1a–c).<sup>[19]</sup> Note that the apparent aggregation of the nano-objects shown in the transmission electron microscopy (TEM) images in Figure 1 is simply a drying artefact, and that both the vesicles and worms are fully dispersed in solution. Here, the PMAA block acts as a steric stabilizer, while the PBzMA block forms the nonsolvated core (if spheres or worms) or membrane (if vesicles). Ionization of the PMAA stabilizer block occurs on transferring such nano-objects from ethanol to water via dialysis, which leads to highly anionic surface character at around pH 9, as judged by aqueous electrophoresis.<sup>[19]</sup>

### 2.1. Synthesis and Incorporation

Calcium carbonate was precipitated in the presence of 20–500 µg mL<sup>-1</sup> copolymer vesicles (PMAA<sub>71</sub>–PBzMA<sub>98</sub>) and copolymer worms (PMAA<sub>71</sub>–PBzMA<sub>300</sub>) using the ammonia diffusion method<sup>[20]</sup> after dispersing the copolymer nano-objects in aqueous Ca<sup>2+</sup> solutions. Calcite single crystals formed under all conditions, except at very high copolymer concentrations (500 µg mL<sup>-1</sup>) or when [Ca<sup>2+</sup>] > 2.5 × 10<sup>-3</sup> M, when intergrown aggregates or polycrystalline calcite particles with dumbbell shapes formed (Figure SI1, Supporting Information). This is consistent with higher concentrations of the polymers retarding crystal growth such that aggregation of crystallites to form polycrystalline particles is faster than their growth as single crystals. The effects of the copolymer nano-objects on the crystal morphologies were assessed by holding the Ca<sup>2+</sup> concentration fixed at 1.25 × 10<sup>-3</sup> M and varying the copolymer concentration from 20 to 500 µg mL<sup>-1</sup>. A sequence of morphological changes in the presence of typical of anionic additives was observed,<sup>[21]</sup> where these varied from perfect rhombohedra at low copolymer concentrations, to rhombohedra with truncated edges as the copolymer concentration increased, to particles elongated along the [001] axis and capped at each apex with three adjacent {104} faces, and ultimately to elongated particles with curved surfaces (Figure 1d–m and Figure SI2, Supporting Information). These morphologies reflect the differing interactions of the additives with the acute and obtuse steps on the exposed {104} faces.<sup>[22]</sup> Both types of copolymer nano-objects had very similar morphological effects.

The occlusion of these nano-objects within calcite single crystal was then investigated. Growth conditions were selected where the crystals exhibited near-rhombohedral morphologies and cross sections for scanning electron microscopy (SEM) and thin sections for transmission electron microscopy (TEM) were prepared using focussed ion beam (FIB) milling. The SEM images confirmed that both worms and vesicles were efficiently occluded throughout the crystals with no evidence of any aggregation or segregation (Figures 2a,b). The cross-section of the vesicle/calcite crystal shows almost perfectly circular occlusions with diameters ranging from 200 to 20 nm, as expected when cross-sectioning vesicles at positions ranging from their centers to their peripheries (Figure 2a). Notably, the maximum observed size is in excellent agreement with the mean vesicle diameter determined by DLS ( $d_{\text{DLS}} = 185$  nm, PDI = 0.16).

Analysis of the worm/calcite crystals also confirmed that the worms retained their structural integrity during occlusion.

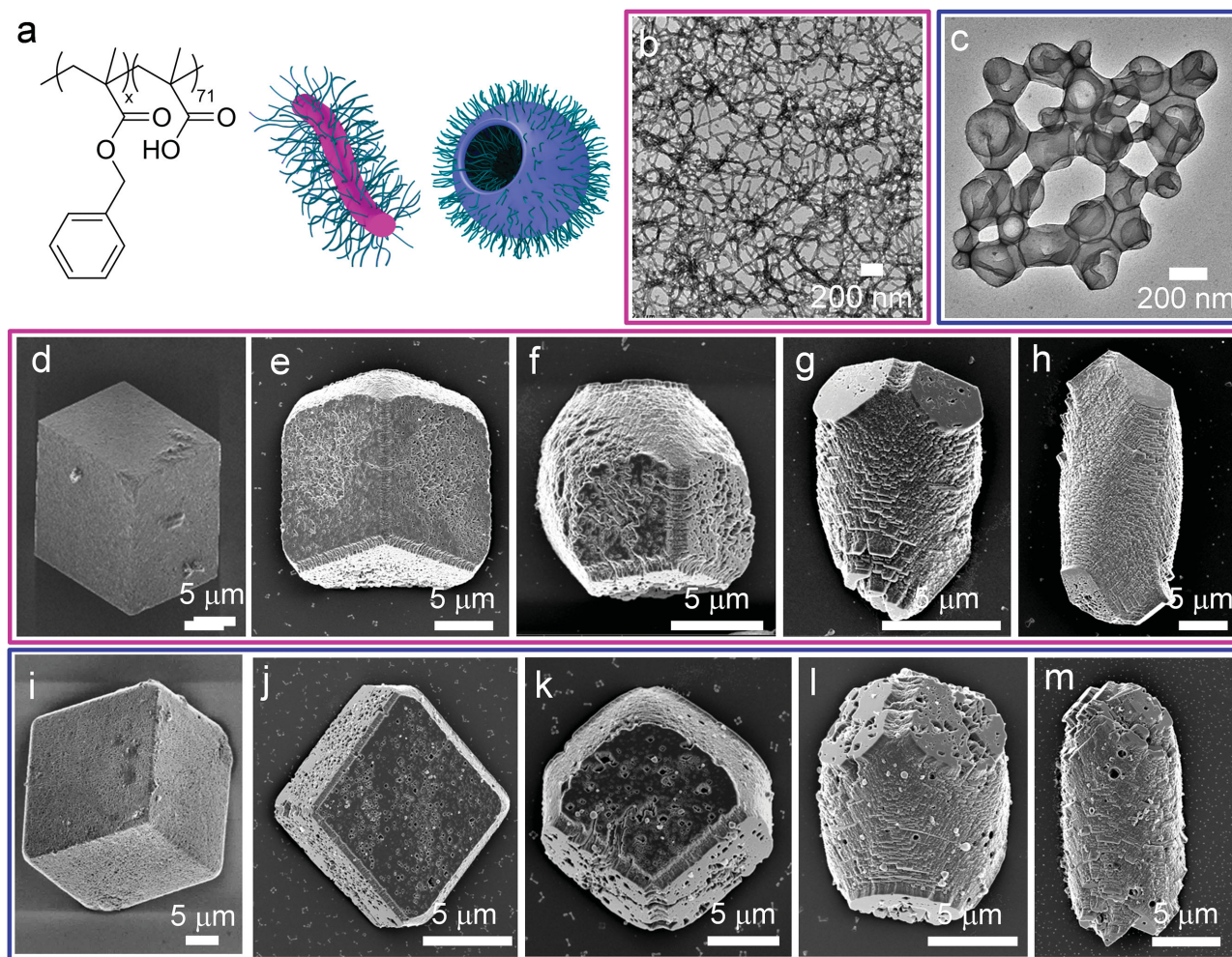


**Figure 1.** a) The chemical structure of the poly(methacrylic acid)-poly(benzyl methacrylate) (PMAA-PBzMA) diblock copolymer particles, where  $x = 98$  and  $y = 71$  for the worm particles and  $x = 300$  and  $y = 71$  for the vesicle particles, and schematics of worm and vesicle nano-objects. b,c) TEM images of (b) copolymer worms and (c) copolymer vesicles. SEM images of calcite crystals precipitated in the presence of d–h) vesicles and i–m) worms at fixed  $[\text{Ca}^{2+}] = 1.25 \times 10^{-3} \text{ M}$  at copolymer concentrations of (d) 20  $\mu\text{g mL}^{-1}$ , (e) 50  $\mu\text{g mL}^{-1}$ , (f) 125  $\mu\text{g mL}^{-1}$ , (g) 250  $\mu\text{g mL}^{-1}$ , (h) 500  $\mu\text{g mL}^{-1}$ , (i) 20  $\mu\text{g mL}^{-1}$ , (j) 50  $\mu\text{g mL}^{-1}$ , (k) 125  $\mu\text{g mL}^{-1}$ , (l) 250  $\mu\text{g mL}^{-1}$ , and (m) 500  $\mu\text{g mL}^{-1}$ , where these show that the crystal morphologies change with increasing copolymer in solution.

SEM analysis of uncoated samples identified worms embedded close to the crystal surface (Figure 2b and Figure S13, Supporting Information), while cross sections showed both circles and elongated structures; the circles occur when a worm is sectioned normal to its long axis (Figure 2b and Figure S13 Supporting Information). This was confirmed by TEM analysis of thin sections of these crystals (Figures 2 c,d), while selected area electron diffraction (SAED) (Figure 2c, inset) and high-resolution TEM (Figure 2d) confirmed single crystal structure. The extents of occlusion of both vesicles and worms within calcite were also quantified using thermogravimetric analysis (TGA) performed under either air or nitrogen, where this showed that both types of copolymer nano-objects were occluded to levels of 15–20 wt% in Figure S14 of the Supporting Information. Occlusion of the polymer nano-objects within calcite single crystals results in a complex decomposition profile as compared with a simple mixture of calcite and polymers, such that it is not possible to obtain a precise estimation of the compositions of the

composite crystals using TGA. A full description of the TGA analysis is provided in the Supporting Information. These values agree well with the volume fractions of about 15% which were estimated from the SEM images (Figures 2a,b). The derivations of the volume fractions are given in the Supporting Information.

Having established that both the copolymer worms and vesicles can be efficiently occluded within calcite single crystals, we then extended our strategy to generate internally patterned calcite crystals. This provides an important proof-of-principle that multifunctional nanocomposite crystals can be formed using this approach. Nanocomposite crystals containing multiple components were readily formed by growing calcite crystals in alternating solutions containing the copolymer worms and vesicles. The crystals were first precipitated from a solution containing only the copolymer worms at  $[\text{Ca}^{2+}] = 1.25 \times 10^{-3} \text{ M}$ , where the supersaturation conditions are such that new calcite crystals nucleate and grow and effective incorporation of the additive can

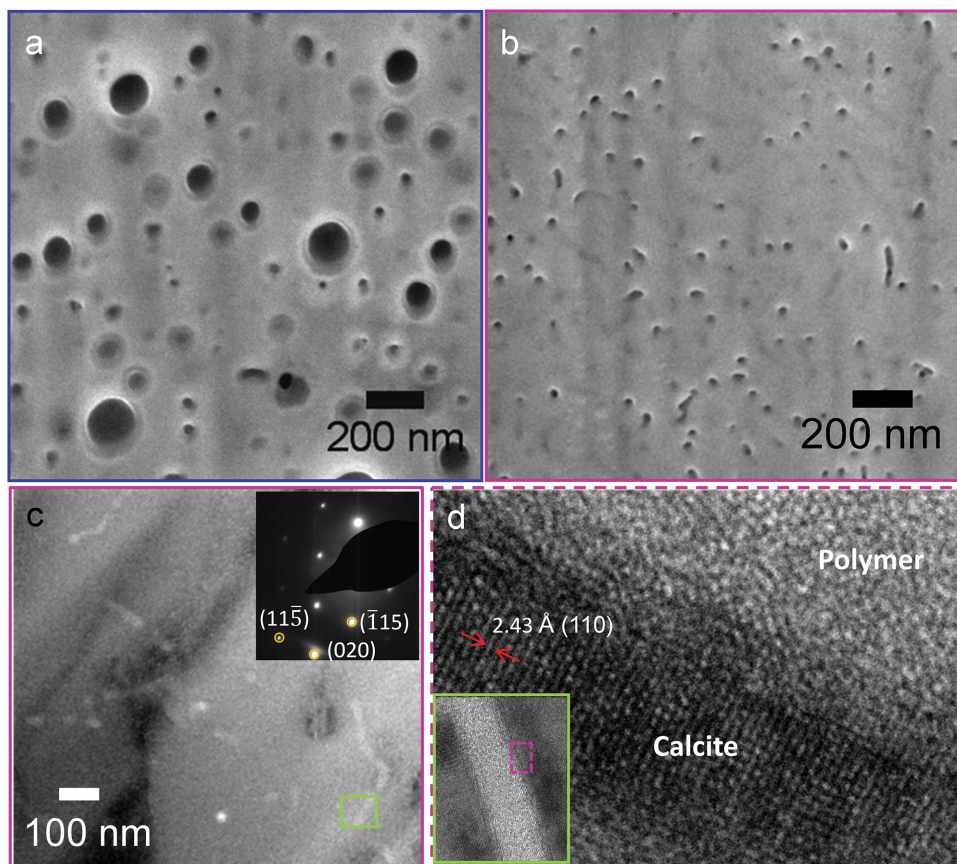


**Figure 2.** a,b) SEM images of cross sections, prepared by FIB, of calcite crystals precipitated at  $[Ca^{2+}] = 1.25 \times 10^{-3} \text{ M}$  in the presence of (a)  $125 \mu\text{g mL}^{-1}$  vesicles and (b)  $125 \mu\text{g mL}^{-1}$  worms, where the occluded particles are uniformly distributed throughout the crystals. c,d) TEM images of thin sections (70–100 nm in thickness), prepared by FIB, of the worm/calcite crystals. The selected area electron diffraction pattern (recorded using a  $1 \mu\text{m}$  aperture) in  $[10\ 0\ 2]$  zone axis (c) shows that the crystal maintains its single crystal structure after occlusion. (d) High magnification images of a single occluded copolymer worm shown in the green box in (c and d) calcite lattice fringes, further confirm the continuity of the lattice.

be achieved. Subsequent exchange of the reaction solution for one of lower supersaturation,  $[Ca^{2+}] = 0.5 \times 10^{-3} \text{ M}$ , then ensured that existing crystals could grow, but that negligible new nucleation events occurred. This created a seamless transition in crystal growth from one reaction solution to the next, such that each growth zone could be set to contain either worms or vesicles (Figure 3a,b). By comparison, when the crystals were precipitated in the presence of a mixture of worms and vesicles (1:2 mol%), the worms were preferentially incorporated, resulting in a random distribution of the two types of nano-objects within the calcite crystals (Figure 3c). This effect is attributed to the higher specific surface area (surface area per unit mass) of the worms as compared with the vesicles, which is expected to aid their occlusion within the calcite crystals. Rough calculations suggest that the worms have specific surface areas of  $114 \text{ m}^2 \text{ g}^{-1}$ , as compared with  $25 \text{ m}^2 \text{ g}^{-1}$  for the vesicles, and comprise 26 wt% charged surface groups as compared with 10 wt% for the vesicles.

## 2.2. Microstructures of the Nanocomposite Crystals

The nanocomposite crystals were analyzed using a number of diffraction and spectroscopic techniques to determine the effect

of the occluded nano-objects on the short-range and long-range structures of the crystals. High resolution synchrotron powder X-ray diffraction (XRD) was used to provide information about the effects of the guest species on the lattice spacings and inhomogeneous strains where this has been shown to be highly specific to the crystal host and the type of occluded species.<sup>[9,13,14]</sup> The data revealed that negligible shifts in the peak positions occurred for either the vesicle/calcite or worm/calcite samples as compared with pure calcite, and that the peaks were nearly symmetric in shape (Figure 4a). Occlusion of the worms and vesicles did however cause some broadening of the peaks, where this was quantified by measuring the peak full-width at half maximum height (FWHM). The ratio of the normalized FWHM (nanocomposite)/FWHM (pure calcite) was 1.55–2.55 for vesicle/calcite and 1.5–2.7 for worm/calcite crystals (as measured for the four main peaks, (110), (104), (006), and (012) (Figure 4c). Analysis of the shapes of the peaks gave coherence lengths of 400–550 nm and 250–350 nm for the vesicle/calcite and worm/calcite crystals respectively, and microstrains of 0.02%–0.03% for both samples (Figure 4d,e). Calcite crystals containing occluded  $0.22\text{--}0.25 \mu\text{m}$  latex particles<sup>[23]</sup> were also analyzed for comparison. No peak shifts and negligible peak broadening was observed such that the normalized FWHM

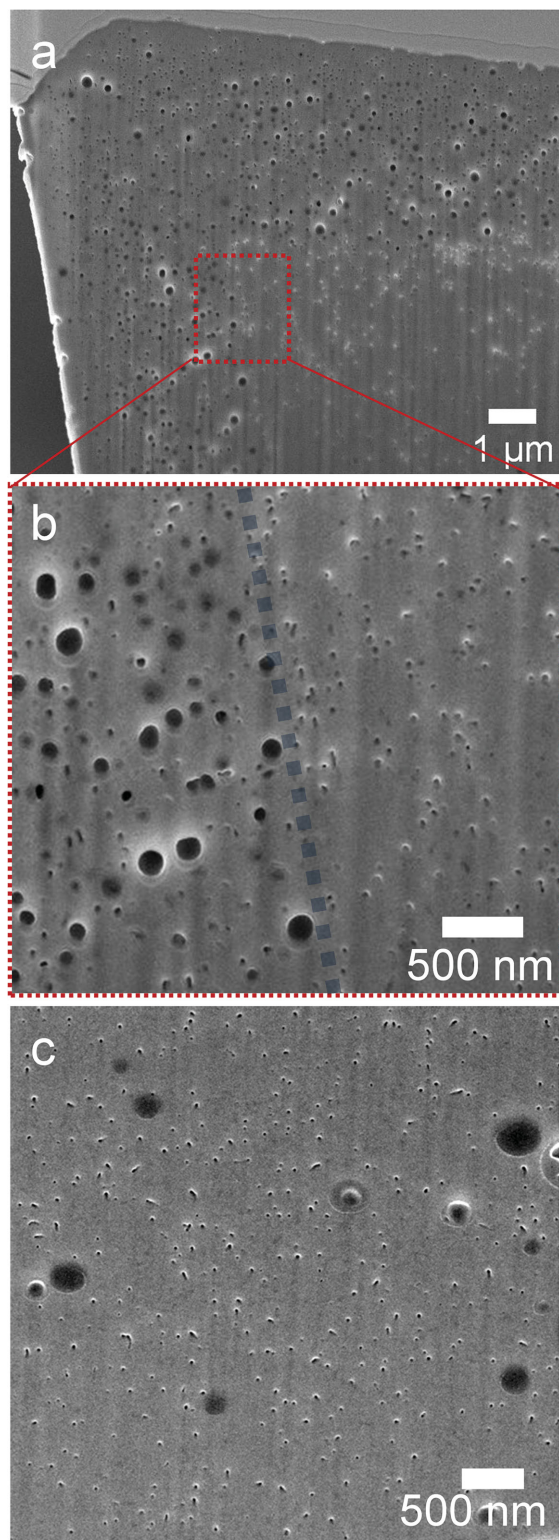


**Figure 3.** SEM images of FIB-cross sectioned calcite crystals precipitated at a,b)  $[Ca^{2+}] = 1.25 \times 10^{-3} \text{ M}$  in the presence of  $125 \mu\text{g mL}^{-1}$  copolymer worms, followed by exchange of the reaction solution to  $[Ca^{2+}] = 0.5 \times 10^{-3} \text{ M}$  and  $125 \mu\text{g mL}^{-1}$  copolymer vesicles where (b) clearly shows the interface between zones containing the two contrasting copolymer particles, and (c) at  $[Ca^{2+}] = 1.25 \times 10^{-3} \text{ M}$  in the presence of a 1:2 mixture (mol%) of copolymer worms and vesicles; a much higher occlusion of copolymer worms is observed.

(nanocomposite)/FWHM (pure calcite) was 1.2 and the coherence length determined from the (104) peak was 558 nm.

Further information about the effect of the copolymer occlusions on the crystal lattice were obtained by recording XRD diffractograms after annealing. Peak broadening is commonly reported on heating both synthetic and biogenic calcite crystals containing occluded organic phases, where this is attributed to the creation of new interfaces.<sup>[9,24,25]</sup> The vesicle/calcite crystals were therefore subjected to isochronous annealing for 30 min at intervals of 100 °C from 100–600 °C and patterns were recorded after the samples had cooled to room temperature after each heating cycle. Peak shifts to smaller  $d$ -values began on heating to 300 °C, where this continues on heating to higher temperatures (Figure 5a,b). The peak broadening also gradually increased up to about 300 °C, and then rose more rapidly above this temperature. The latex/calcite and worm/calcite crystals were analyzed after ex situ heating to 400 °C and showed some differences in behavior as compared with the vesicle/calcite crystals (Figure 5c–e). The latex/calcite crystals showed significantly more broadening than the vesicle/calcite crystals at 400 °C, while the worm/calcite sample showed little broadening. Neither exhibited any significant shift in the peaks. These differences may reflect variations in the degradation behavior of the organic occlusions and in the interfaces between the occlusions and the crystal host.

Raman and IR studies were also performed to determine the influence of the organic occlusions on the ordering of the calcite crystal lattice at the atomic scale. The raman spectra showed broadening of the  $\nu_1$  and  $\nu_4$  peaks, corresponding to the carbonate symmetric stretch and symmetric bend, respectively, as well as the two lattice modes at 279 and 158  $\text{cm}^{-1}$  (Figure 6a,b). This effect was greater for the vesicle/calcite crystals and is indicative of greater short-range disorder in the structure. The IR spectra also revealed increases in the intensity ratio of the  $\nu_2/\nu_4$  peaks from 2.0 for pure calcite to 3.1 and 3.4 for the worm/calcite and vesicle/calcite crystals, respectively (Figure 6b,c). For comparison, a previously reported copolymer micelle/calcite crystal exhibited a  $\nu_2/\nu_4$  ratio of 4.1.<sup>[9]</sup>

### 2.3. Mechanical Properties of the Nanocomposite Crystals

Single crystal calcite biominerals are well known to exhibit increased hardness and toughness as compared to pure synthetic or geological calcite, where this can be attributed to the occlusion of organic biomacromolecules and  $Mg^{2+}$  ions within the calcite lattice.<sup>[26–28]</sup> Characterization of synthetic organic/calcite crystals enables isolation of the hardening effects of just organic occlusions to be studied in the *absence* of ionic substitutions, such as  $Mg^{2+}$ , a well-known hardening agent of calcite.<sup>[27]</sup> The mechanical properties of the worm/calcite and vesicle/calcite crystals were investigated using nanoindentation and were compared with a pure calcite control. These nanocomposite systems provide compositionally and structurally unique systems, where the vesicles contain a significant volume of water in their cores, and the worms have highly anisotropic morphologies. The average hardness and indentation moduli of these crystals are plotted in Figure 7. The consistent standard deviation associated with these measurements can be attributed

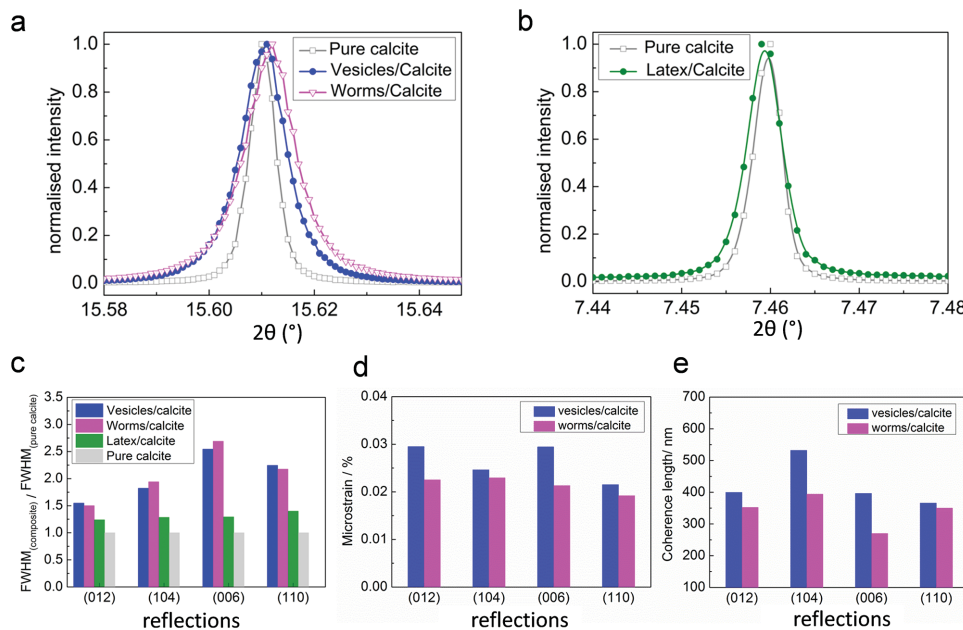


**Figure 4.** High resolution synchrotron powder XRD spectra. a) Profiles of (104) reflections of worm/calcite (pink line) and vesicle/calcite (blue line) crystals. b) Profile of (104) reflection of latex/calcite crystals. c) Ratio of the normalized FWHM of the nanocomposite crystals to the normalized FWHM of pure calcite, d) microstrain, and e) coherence lengths as measured from (012), (104), (006), and (110) reflections.

to the mechanical anisotropy of calcite, and the range of orientations of the crystals studied.<sup>[28]</sup> The values for the calcite control sample closely match those reported for pure geologic calcite,<sup>[28]</sup> and synthetic calcite.<sup>[9]</sup> Both types of nanocomposite crystals were significantly harder than pure calcite, while the indentation modulus was reduced as compared with this reference material. The worm/calcite crystals exhibited the largest increase in hardness (+24%) and the smallest reduction in modulus (−5%), as compared to +16% and −15% values for the vesicle/calcite crystals. These data can also be compared with calcite occluding 9.3 wt% of 250 nm carboxylated polystyrene latex particles which were ≈30% less hard than pure calcite,<sup>[23]</sup> while calcite incorporating 13 wt% of 20 nm block copolymer micelles were ≈16% harder than pure calcite.<sup>[9,23]</sup>

#### 2.4. In Situ Observation of the Incorporation of Copolymer Worms in Calcite

The mechanisms by which the copolymer worms become incorporated within the growing calcite crystals were studied using in situ atomic force microscopy (AFM). As the worms are significantly larger than the 3.1 nm step edges on calcite, it was challenging to simultaneously image both the step edges and the worms. The worms were first imaged on the surface of mica (rendered cationic via electrostatic adsorption of poly(L-lysine)) in order to characterize their morphologies and the data were in good agreement with TEM images of dried worms (Figure S15, Supporting Information). Growth experiments were then performed by imaging the changes that occur on the exposed {104} surface of a freshly cleaved single crystal of geological calcite when it is exposed to the reaction solution within a commercial fluid cell.<sup>[29]</sup> The copolymer worms strongly

adsorbed to the crystal substrate in a random distribution and did not change position on coming in contact with the propagating steps during crystal growth (Figure 8a). Notably, while the worms became progressively buried during crystal growth, the crystal did not immediately “heal over” the buried worms, such that deep voids formed above them. This behavior was more pronounced for larger voids (Figure 8a, navy arrow).

Such voids have previously been observed in a detailed study of the occlusion of 20 nm anionic copolymer micelles within calcite single crystals.<sup>[29]</sup> Cavity formation can be attributed to the partly buried nanoparticle straining the surrounding crystal, which reduces the driving force for crystallization and contributes to the formation of a cavity. The difficulty of extending the crystal steps over the surface of the underlying occlusion may also contribute to cavity formation. Imaging of crystal growth after a worm had attached to the surface also revealed a second interesting feature (Figure 8b). When new worms adsorbed to an existing void, or another worm, they readily detached and returned to the solution (red and turquoise arrows in Figure 8b). This indicates a reduced adsorption strength as compared to direct binding to the calcite surface, where this prevents the occlusion of these loosely bound worms within the crystal.

### 3. Discussion

Much of our current knowledge about the occlusion of organic additives within single crystals has come from the study of calcite biominerals and synthetic calcite crystals precipitated in the presence of macromolecules extracted from biominerals. Some of the earliest work characterized single crystal calcite biominerals such as sea urchin larval spicules,<sup>[7,30]</sup> and revealed that

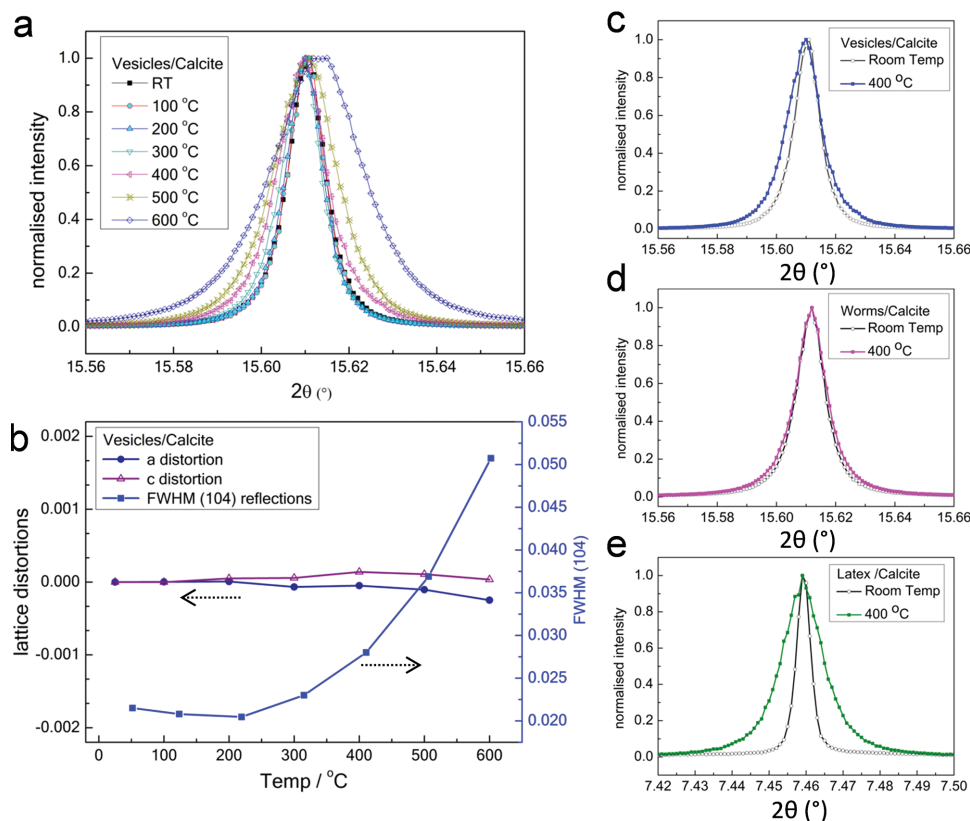


**Figure 5.** High resolution synchrotron powder XRD spectra of worm/calcite and vesicle/calcite crystals. a) The change in the (104) reflection of a vesicle/calcite crystal recorded after annealing at temperatures between 100 and 600 °C for 30 min, where a marked broadening occurs from 300 °C. b) The measured broadening and *a*-axis and *c*-axis lattice distortion of the (104) reflections shown in (a), where data were obtained using line profile analysis and Rietveld analysis. c–e) Change in profiles of (104) reflections of (c) vesicle/calcite, (d) worm/calcite, and (e) latex/calcite after annealing at 400 °C, where these are compared with the same samples measured at room temperature (gray line).

the domain size and shape in many ways mirrored the gross morphologies of these biominerals. This was attributed to selective binding of the constituent macromolecules to specific lattice planes and a similar pattern of binding was obtained with synthetic crystals precipitated in the presence of extracted macromolecules.<sup>[31]</sup> These studies therefore suggest that variations in the structures of the occluded organic macromolecules can result in different crystal microstructures and textures.

Powder diffraction studies comparable to those performed here have also been used to study calcite biominerals, although analysis of the peak shape and position are complicated by the inevitable presence of magnesium.<sup>[25,32]</sup> Nevertheless, comparison of the calcite prisms from a range of mollusks has revealed species-specific variations in the microstrain and macrostrain,<sup>[25,33]</sup> where these have been attributed to differences in the compositions of the macromolecules, rather than the amounts occluded.<sup>[34]</sup> Investigations have therefore often focused on calcite crystals coprecipitated with extracted molecules, where XRD spectra from calcite crystals occluding the small protein perlucin<sup>[24]</sup> showed smaller peak shifts than calcite precipitated in the presence of “caspartin,” a 17 kDa protein extracted from the calcitic prisms of *Pinna nobilis*.<sup>[32]</sup>

Purely synthetic systems—such as the copolymer worms and vesicles studied here—offer an alternative and effective strategy for determining the relationship between the chemical

structure, size, and shape of additives and the structure and properties of nanocomposite crystals. Ions and small molecules such as Mg<sup>2+</sup> and amino acids have dramatic effects on the host crystal lattice, causing both peak shift and broadening. Taking the example of the amino acids, the broadening appears to correlate with the degree of peak shift, and changes from isotropic to anisotropic with greater peak shifts.<sup>[13]</sup> Larger species such as anionic polyelectrolytes,<sup>[35]</sup> and the worms and vesicles investigated here, in contrast, cause broadening but little peak shift. The negligible peak shifts observed in the calcite crystals occluding copolymer worms, vesicles or micelles therefore suggest that the inhomogeneous strains introduced by the copolymer nano-objects are either not significant enough, or that the inclusions are too localized to generate lattice distortions. The form of the microstrain also varies considerably according to the type of occlusion. Calcite occluding 20 nm anionic block copolymer micelles exhibited highly anisotropic XRD peaks consistent with a compressive strain gradient around the particles,<sup>[9]</sup> while the peaks from the vesicle/calcite and worm/calcite samples showed greater—but isotropic peak broadening.

These data demonstrate that multiple factors dictate how occluded species affect the crystal lattice. Ions and small molecules are present in the lattice as solutes, directly replacing host ions. A misfit results in local strain, and with sufficient occluded species, changes in the average lattice spacings. That

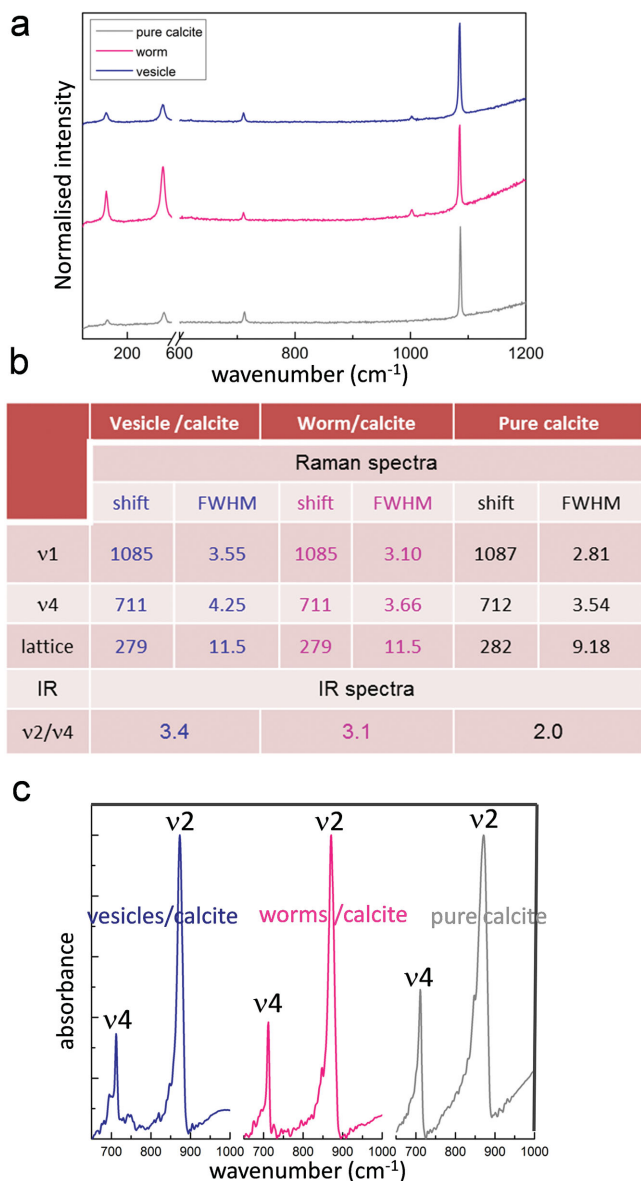


**Figure 6.** a) Raman spectra of worm/calcite and vesicle/calcite crystals. As summarized in b), these show the signature peaks of calcite, where these are broadened as compared with pure synthetic calcite, but show negligible shift. The  $v_1$  and  $v_4$  peaks correspond to the  $\text{CO}_3^{2-}$  symmetric stretch and symmetric bending respectively, and two lattice mode peaks are also shown. c) IR spectra of worm/calcite and vesicle/calcite crystals, which show that the height ratio of the  $v_2/v_4$  peaks measured at  $v_2$  ( $874\text{--}878\text{ cm}^{-1}$ ) and  $v_4$  ( $710\text{--}715\text{ cm}^{-1}$ ) increase from 2.0 (pure calcite) to 3.1 (worm) and 3.4 (vesicle), respectively.

biominerals show both peak broadening and lattice distortion suggests that the occluded macromolecules may at least partly behave as solute species. At the opposite end of the spectrum, latex particles had little effect on the crystal lattice — either on peak position or broadening — and thus behave as second-phase particles. Notably, however, the vesicle/calcite samples do show broadening, despite the vesicles and latexes having comparable sizes.

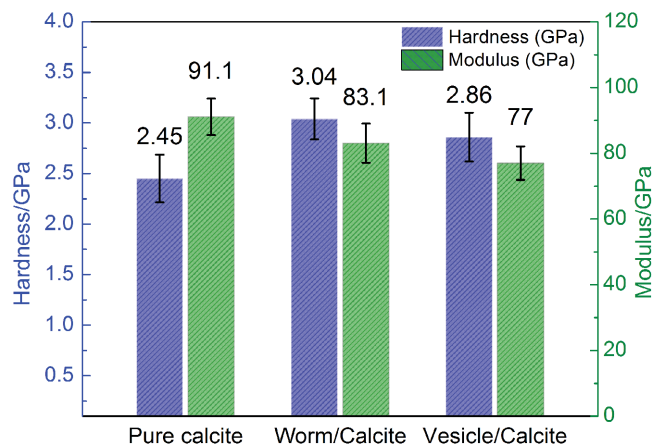


**Figure 7.** Hardness and indentation modulus of worm/calcite and vesicle/calcite single crystals, as compared with pure calcite crystals, measured using nanoindentation.

The effect of an occlusion on the crystal lattice is therefore not simply dependent on its size. Factors such as the structure of the crystal/organic interface must also be important, where this is likely to depend on the physical properties of the occluded particles. Indeed, the vesicles and worms are more compliant than the latexes, such that they flatten somewhat on the crystal surface to maximize the interaction (as seen by AFM). This effect is not large enough to change the overall shape of the nano-object on occlusion, as shown in Figures 2a and 2b. It is also noted that block copolymer micelles, which comprise 41 wt% of a charged corona, exerted a much greater effect on the crystal lattice than the vesicles and worms, which comprise 10 and 26 wt% of charged surface groups, respectively. The specific compositions and conformations of the occlusion-species therefore not only govern the efficiency of incorporation, but also play significant roles in determining the effects of the occlusions on the crystal lattice.

The occluded worms and vesicles also affect the physical properties of the nanocomposite crystals. The hardness of the copolymer/calcite crystals studied here — where the worm/calcite crystals were somewhat harder than the vesicle/calcite crystals — is a measure of the resistance of the material to plastic deformation and thus to the motion of dislocations in the crystal lattice. The incorporated soft copolymer could increase hardness by blocking dislocation motion either by forcing dislocations to directly intersect an incorporated copolymer region, or by interacting with any heterogeneous strain fields that might surround the copolymer inclusions.<sup>[36]</sup> The magnitude of this hardening should correlate with the inverse of the average spacing between the copolymers inclusions.<sup>[37]</sup> Rough calculations based on the analysis of SEM images of the cross sections of the calcite crystals occluding worms and vesicles demonstrated no significant difference in the average spacings. However, since the worms are long and slender, they have a much larger capture cross-section for dislocations than this simple spacing would suggest. This is also consistent with the shorter coherence length of the worm/calcite crystals. It is also noted that the latex/calcite crystals were less hard than pure calcite, despite showing comparable coherence lengths and particle

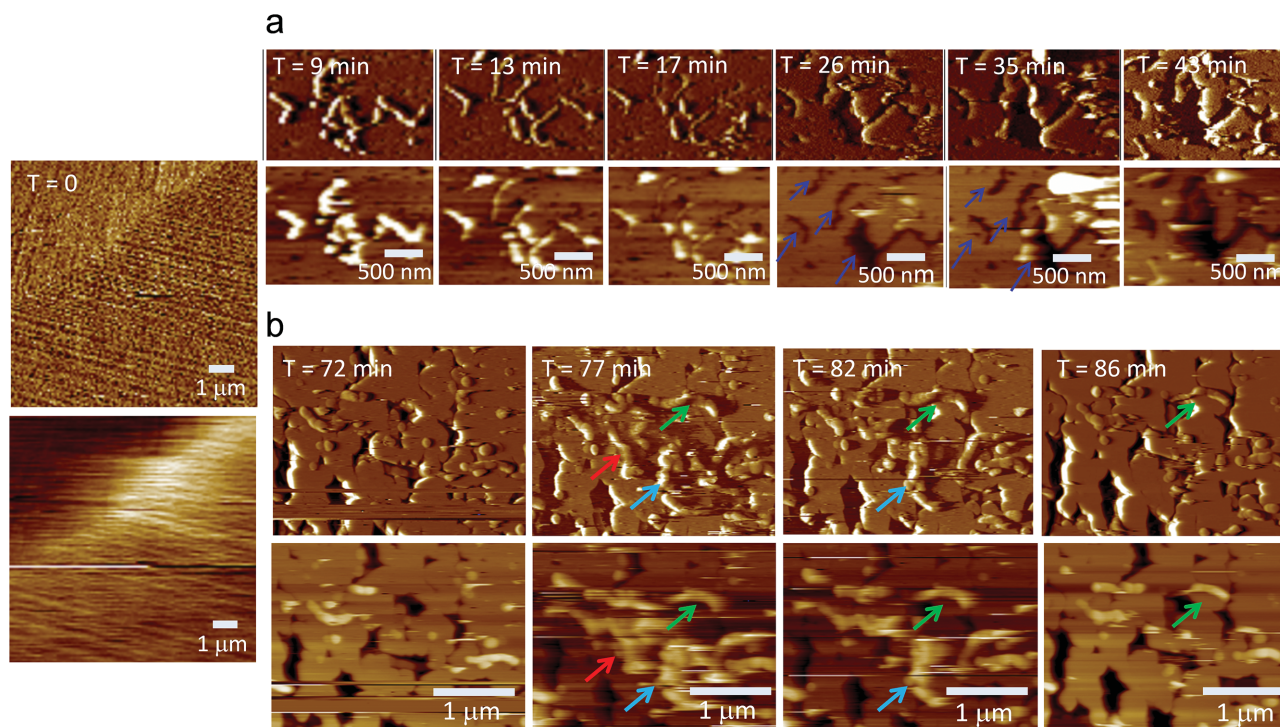


**Figure 8.** AFM deflection (top) and height images (bottom) recorded in situ during crystal growth in the presence of copolymer worm particles. The bare calcite crystal showing surface steps is shown on the left hand side, labeled as  $T = 0$ . a) A series of images, recorded at the times indicated, showing the initial adsorption and then gradual occlusion of the worms within the calcite crystal. The images also demonstrate that voids are formed immediately after burial of the worms (navy arrows at  $T = 26$  and  $35$  min). b) Images recorded on a different area, which show the occlusion of a copolymer worm that is directly adsorbed to the calcite surface (green arrow). Worms adsorbed to voids or other adsorbed worms become detached rather than being occluded (red and turquoise arrows).

separations to the vesicle/calcite crystals. As the former sample showed significantly less microstrain than the latter, this suggests that the local strain fields may also contribute to the hardening of the nanocomposite crystals.

The modulus, in turn, is a measure of the elastic response of the whole nanocomposite, such that addition of a relatively compliant copolymer should decrease the modulus of the nanocomposite by an amount that correlates with the volume fraction of the incorporated copolymer.<sup>[38]</sup> All of the nanocomposite crystals examined exhibited lower moduli than pure calcite, with a reduction of  $\approx 10\%$  for the worm/calcite crystals and  $\approx 15\%$  for vesicle/calcite crystals. The larger volume fraction of the vesicles than worms is consistent with the lower modulus in the worm/calcite samples. While an accurate calculation would require knowledge of both the volume fraction and the modulus of the occluded copolymer, the moduli of the copolymer inclusions are expected to be orders of magnitude lower than that of calcite, so that to first order, the volume fraction dominates.

#### 4. Conclusions

The work described here demonstrates that the rational design of diblock copolymer nano-objects not only promotes their incorporation within single crystals, but can also be used to control the structure and properties of the product crystals. In

combination with our previous data on the occlusion of copolymer micelles<sup>[9]</sup> and anionic polymer latexes<sup>[23]</sup> in calcite, it is shown that particles that vary widely in size (20 nm spheres and 500 nm vesicles) and shape (isotropic spheres versus anisotropic worms) can be efficiently occluded by functionalizing the particles with a corona comprising multiple anionic carboxylate groups. This approach can also be extended to create internally patterned crystals in which different zones contain different copolymer nano-objects. As a key finding of our study, we show that the influence of these occlusions on the crystal lattice, as indicated by changes in the peak position and shape of powder X-ray diffractograms, depends on the structure of the particles. While the calcite lattice remains virtually unaffected by the occlusion of 250 nm polystyrene particles, isotropic microstrains arise from the incorporation of copolymer worms and vesicles. Occlusion of the copolymers also had significant effects on mechanical properties where both worms and vesicles led to increased hardness and reduced modulus, despite the very different morphologies of the inclusions. Finally, the occlusion of vesicles within single calcite crystals has broader interest. These systems have enormous potential for further functionalization, which could be achieved by introducing functional molecules (e.g., proteins or enzymes) or nanoparticles into the polymer assemblies. This would open the door to a new generic strategy for the occlusion of payloads that do not have any intrinsic affinity for the crystal lattice.

## 5. Experimental Section

Calcium carbonate was precipitated in the presence of the copolymer worms and copolymer vesicles using the ammonium diffusion method.<sup>[20]</sup> Stock solutions of copolymers were added to a solution of  $\text{CaCl}_2 \cdot 2\text{H}_2\text{O}$  ( $0.5 \times 10^{-3}$ – $5 \times 10^{-3}$  M) to form final solutions with copolymers ( $5$ – $500 \mu\text{g mL}^{-1}$ ). Crystallization was typically allowed to proceed for 1 d (unless stated otherwise). Following this period, the glass slides supporting the  $\text{CaCO}_3$  crystals were removed from the solutions, were washed with Millipore water and ethanol, then were dried in air to be analyzed using high resolution powder XRD, optical microscopy, SEM, TEM, IR spectroscopy, Raman microscopy, and TGA. For comparison, experiments were also performed by precipitating  $\text{CaCO}_3$  in the presence of commercial, functionalized latex particles, as described in previous work.<sup>[23]</sup> High acid content particles that were  $0.22$ – $0.25 \mu\text{m}$  in size and which exhibited a corona of flexible chains were purchased from Bangs Labs Inc. (IN, USA).

## Supporting Information

Supporting Information is available from the Wiley Online Library or from the author.

## Acknowledgements

This project was supported by a grant from the US National Science Foundation (Materials Word Network Award DMR 1210304), an Engineering and Physical Sciences Research Council (EPSRC) Leadership Fellowship (F.C.M. and YYK, EP/H005374/1), and EPSRC grants EP/J018589/1 (Materials World Network, F.C.M. and Y.Y.K.) and EP/K006304/1 (F.C.M. and A.N.K.). Work at the Molecular Foundry was supported by the Office of Science, Office of Basic Energy Sciences, of the U.S. Department of Energy under Contract No. DE-AC02-05CH11231. The work was further supported by Hysitron Inc, (Edina, MN, USA). The authors acknowledge Diamond Light Source for time on beamline I11 under commissioning time and proposal EE10137. The authors would also like to thank Prof. Jim De Yoreo for providing access to AFM facilities and for giving useful advice, and Andre H. Groschel for providing the copolymer schematics.

Received: October 7, 2015

Revised: November 18, 2015

Published online: January 28, 2016

- [1] S. Srivastava, N. A. Kotov, *Acc. Chem. Res.* **2008**, *41*, 1831.
- [2] a) Y. B. Fan, P. Upadhyaya, X. F. Kou, M. R. Lang, S. Takei, Z. X. Wang, J. S. Tang, L. He, L. T. Chang, M. Montazeri, G. Q. Yu, W. J. Jiang, T. X. Nie, R. N. Schwartz, Y. Tserkovnyak, K. L. Wang, *Nat. Mater.* **2014**, *13*, 699; b) I. M. Miron, G. Gaudin, S. Auffret, B. Rodmacq, A. Schuhl, S. Pizzini, J. Vogel, P. Gambardella, *Nat. Mater.* **2010**, *9*, 230.
- [3] a) M. Cargnello, B. T. Diroll, E. A. Gaulding, C. B. Murray, *Adv. Mater.* **2014**, *26*, 2419; b) A. G. Dong, X. C. Ye, J. Chen, C. B. Murray, *Nano Lett.* **2011**, *11*, 1804; c) E. V. Shevchenko, D. V. Talapin, N. A. Kotov, S. O'Brien, C. B. Murray, *Nature* **2006**, *439*, 55.
- [4] a) B. Sarkar, P. Alexandridis, *Prog. Polym. Sci.* **2015**, *40*, 33; b) Y. Zhao, K. Thorkelsson, A. J. Mastroianni, T. Schilling, J. M. Luther, B. J. Rancatore, K. Matsunaga, H. Jinnai, Y. Wu, D. Poulsen, J. M. J. Frechet, A. P. Alivisatos, T. Xu, *Nat. Mater.* **2009**, *8*, 979.
- [5] B. Kahr, R. W. Gurney, *Chem. Rev.* **2001**, *101*, 893.
- [6] a) H. A. Lowenstam, S. Weiner, *On Biomineralization*, Oxford University Press, New York **1989**; b) E. Weber, B. Pokroy, *CrystEngComm* **2015**, *17*, 5873.
- [7] A. Berman, J. Hanson, L. Leiserowitz, T. F. Koetzle, S. Weiner, L. Addadi, *Science* **1993**, *259*, 776.
- [8] J. W. C. Dunlop, P. Fratzl, *Annu. Rev. Mater. Res.* **2010**, *40*, 1.
- [9] Y. Y. Kim, K. Ganesan, P. Yang, A. N. Kulak, S. Borukhin, S. Pechook, L. Ribeiro, R. Kröger, S. J. Eichhorn, S. P. Armes, B. Pokroy, F. C. Meldrum, *Nat. Mater.* **2011**, *10*, 890.
- [10] a) A. N. Kulak, M. Semsarilar, Y. Y. Kim, J. Ihli, L. A. Fielding, O. Cespedes, S. P. Armes, F. C. Meldrum, *Chem. Sci.* **2014**, *5*, 738; b) A. N. Kulak, P. C. Yang, Y. Y. Kim, S. P. Armes, F. C. Meldrum, *Chem. Commun.* **2014**, *50*, 67.
- [11] a) R. Munoz-Espi, G. Jeschke, I. Lieberwirth, C. M. Gomez, G. Wegner, *J. Phys. Chem. B* **2007**, *111*, 697; b) Y. Ning, L. A. Fielding, T. S. Andrews, D. J. Gowney, S. P. Armes, *Nanoscale* **2015**, *7*, 6691.
- [12] M. Adam, Z. Wang, A. Dubavik, G. M. Stachowski, C. Meerbach, Z. Soran-Erdem, C. Rengers, H. Volkan-Demir, N. Gaponik, A. Eychmüller, *Adv. Funct. Mater.* **2015**, *25*, 2638.
- [13] S. Borukhin, L. Bloch, T. Radlauer, A. H. Hill, A. N. Fitch, B. Pokroy, *Adv. Funct. Mater.* **2012**, *22*, 4216.
- [14] A. Brif, G. Ankonina, C. Drathen, B. Pokroy, *Adv. Mater.* **2014**, *26*, 477.
- [15] a) D. E. Discher, A. Eisenberg, *Science* **2002**, *297*, 967; b) B. M. Discher, Y. Y. Won, D. S. Ege, J. C. M. Lee, F. S. Bates, D. E. Discher, D. A. Hammer, *Science* **1999**, *284*, 1143; c) Y. Y. Won, H. T. Davis, F. S. Bates, *Science* **1999**, *283*, 960; d) L. F. Zhang, A. Eisenberg, *Science* **1995**, *268*, 1728.
- [16] a) N. J. Warren, S. P. Armes, *J. Am. Chem. Soc.* **2014**, *136*, 10174; b) A. Blanazs, J. Madsen, G. Battaglia, A. J. Ryan, S. P. Armes, *J. Am. Chem. Soc.* **2011**, *133*, 16581.
- [17] a) C. Gonzato, M. Semsarilar, E. R. Jones, F. Li, G. J. P. Krooshof, P. Wyman, O. O. Mykhaylyk, R. Tuinier, S. P. Armes, *J. Am. Chem. Soc.* **2014**, *136*, 11100; b) M. Semsarilar, E. R. Jones, A. Blanazs, S. P. Armes, *Adv. Mater.* **2012**, *24*, 3378.
- [18] a) L. A. Fielding, J. A. Lane, M. J. Derry, O. O. Mykhaylyk, S. P. Armes, *J. Am. Chem. Soc.* **2014**, *136*, 5790; b) L. A. Fielding, M. J. Derry, V. Ladmiral, J. Rosselgong, A. M. Rodrigues, L. P. D. Ratcliffe, S. Sugihara, S. P. Armes, *Chem. Sci.* **2013**, *4*, 2081.
- [19] M. Semsarilar, V. Ladmiral, A. Blanazs, S. P. Armes, *Polym. Chem.* **2014**, *5*, 3466.
- [20] J. Ihli, P. Bots, A. Kulak, L. G. Benning, F. C. Meldrum, *Adv. Funct. Mater.* **2013**, *23*, 1965.
- [21] a) Y. Y. Kim, A. S. Schenk, J. Ihli, A. N. Kulak, N. B. J. Hetherington, C. C. Tang, W. W. Schmahl, E. Griesshaber, G. Hyett, F. C. Meldrum, *Nat. Commun.* **2014**, *5*, 4341; b) C. L. Chen, J. H. Qi, J. H. Tao, R. N. Zuckermann, J. J. DeYoreo, *Sci. Rep.* **2014**, *4*, 6266.
- [22] C. A. Orme, A. Noy, A. Wierzbicki, M. T. McBride, M. Grantham, H. H. Teng, P. M. Dove, J. J. DeYoreo, *Nature* **2001**, *411*, 775.
- [23] Y. Y. Kim, L. Ribeiro, F. Maillot, O. Ward, S. J. Eichhorn, F. C. Meldrum, *Adv. Mater.* **2010**, *22*, 2082.
- [24] E. Weber, L. Bloch, C. Guth, A. N. Fitch, I. M. Weiss, B. Pokroy, *Chem. Mater.* **2014**, *26*, 4925.
- [25] B. Pokroy, A. N. Fitch, E. Zolotoyabko, *Adv. Mater.* **2006**, *18*, 2363.
- [26] S. Weiner, L. Addadi, H. D. Wagner, *Mater. Sci. Eng., C* **2000**, *11*, 1.
- [27] M. E. Kunitake, S. P. Baker, L. A. Estroff, *MRS Commun.* **2012**, *2*, 113.
- [28] M. E. Kunitake, L. M. Mangano, J. M. Peloquin, S. P. Baker, L. A. Estroff, *Acta Biomater.* **2013**, *9*, 5353.
- [29] K. R. Cho, Y. Y. Kim, P. Yang, W. Cai, H. Pan, A. N. Kulak, J. L. Lau, P. Kulshreshtha, S. P. Armes, F. C. Meldrum, J. J. DeYoreo, *Nat. Commun.* **2016**, *9*, 10187.

- [30] A. Berman, L. Addadi, A. Kvik, L. Leiserowitz, M. Nelson, S. Weiner, *Science* **1990**, *250*, 664.
- [31] a) S. Albeck, J. Aizenberg, L. Addadi, S. Weiner, *J. Am. Chem. Soc.* **1993**, *115*, 11691; b) J. Aizenberg, J. Hanson, T. F. Koetzle, S. Weiner, L. Addadi, *J. Am. Chem. Soc.* **1997**, *119*, 881.
- [32] B. Pokroy, A. N. Fitch, F. Marin, M. Kapon, N. Adir, E. Zolotoyabko, *J. Struct. Biol.* **2006**, *155*, 96.
- [33] E. Zolotoyabko, E. N. Caspi, J. S. Fieramosca, R. B. Von Dreele, F. Marin, G. Mor, L. Addadi, S. Weiner, Y. Politi, *Cryst. Growth Des.* **2010**, *10*, 1207.
- [34] T. Okumura, M. Suzuki, H. Nagasawa, T. Kogure, *J. Cryst. Growth* **2013**, *381*, 114.
- [35] A. S. Schenk, I. Zlotnikov, B. Pokroy, N. Gierlinger, A. Masic, P. Zaslansky, A. N. Fitch, O. Paris, T. H. Metzger, H. Colfen, P. Fratzl, B. Aichmayer, *Adv. Funct. Mater.* **2012**, *22*, 4668.
- [36] R. L. Fleischer, *Acta Metall.* **1961**, *9*, 996.
- [37] J. Pelleg, *Mechanical Properties of Ceramics*, Springer International Publishing, Basel, **2014**.
- [38] H. S. Kim, S. I. Hong, S. J. Kim, *J. Mater. Process. Technol.* **2001**, *112*, 109.